IEEE Access
Multidisciplinary | Rapid Review | Open Access Journal

Received 3 July 2022, accepted 20 July 2022, date of publication 26 July 2022, date of current version 3 August 2022.

Digital Object Identifier 10.1109/ACCESS.2022.3194015

RESEARCH ARTICLE

Toward Practical Temporal Diversity Coherent Combining Based Variable Data-Rate Free Space Optical Communication Systems

FAMING LI[1,2], SHENG CUI[1,2], YANAN CHEN[3], CHENJIE RAO[4], YICONG TU[1,2], KEJI ZHOU[4], AND DEMING LIU[1,2]

[1]Wuhan National Laboratory for Optoelectronics, School of Optical and Electronic Information, Huazhong University of Science and Technology, Wuhan 430074, China
[2]National Engineering Laboratory for Next Generation Internet Access System, Wuhan 430074, China
[3]Science and Technology on Electro-Optical Information Security Control Laboratory, Tianjin 300308, China
[4]Fiberhome Telecommunication Technologies Company Ltd., China Information Communication Technologies Group Corporation, Wuhan 430074, China

Corresponding author: Sheng Cui (cuisheng@hust.edu.cn)

This work was supported by the National Natural Science Foundation of China (NSFC) under Grant 61975059 and Grant 61975063.

ABSTRACT Free-space optical communication (FSOC) systems with variable data-rates can support different missions with different transmission distances and ensure reliable transmission in periods of unfavorable weather conditions. The temporal diversity coherent combining (TDCC) technique can adjust the data-rate in a very large range using a software-defined manner by taking advantage of the digital coherent receivers able to recover the signal field. In this paper, we investigate the relationships between the computational complexity, optical phase alignment error, combining loss (CL) and data-rate for the TDCC-based variable data-rate coherent optical receiver. We also propose a method to minimize the computational complexity while achieving the expected output optical signal-to-noise ratio (OSNR) and the highest data-rate for an arbitrary input OSNR. Numerical simulations and experiments are carried out to validate the analytical expressions and proposed methods. The results provide an efficient tool and useful guidelines for the design of low computation complexity TDCC-based variable data-rate FSOC systems.

INDEX TERMS Temporal diversity coherent combining, free-space optical communication, variable data rate, phase alignment, combining loss.

I. INTRODUCTION

The free-space optical communication (FSOC) system with unregulated spectrum, ultra-large capacity, and small size, weight and power consumption (SWaP) is an ideal candidate for inter-satellite, earth-to-satellite, data centers, backhaul and fronthaul communications [1]–[4]. An ideal FSOC system should be able to support a wide diversity of missions with different rates and reaches, and ensure reliable transmission in periods of unfavorable weather conditions [2], [5]. Instead of designing a specialized transceiver or modifying the hardware architecture for each scenario, a more cost-effective and practical approach is to design a variable data-rate transceiver able to trade rates for loss tolerance in a software-defined manner.

By now, various rate-scaling techniques have been proposed. Changing the baud rate is straightforward but not practical due to hardware limitations, as the optical filter bandwidth, DSP circuit working frequency, parallel factor and hardware architecture are hard to change. By now, the rate-scaling techniques proposed include but are not limited to changing the modulation order of the m-ary pulse-position modulation (m-PPM) [6], phase-shift keying (m-PSK) [7] and quadrature amplitude modulation (m-QAM) signals [8], altering the slot rate of the m-PPM signals [9], controlling the duty cycle of the burst-rate m-PPM signals [10] and differential phase-shift keying (DPSK) signals [11], [12], varying the forward error correction (FEC) code rate [7] and modifying

The associate editor coordinating the review of this manuscript and approving it for publication was Faissal El Bouanani.

This work is licensed under a Creative Commons Attribution 4.0 License. For more information, see https://creativecommons.org/licenses/by/4.0/

the probabilistic constellation shaping (PCS) M-QAM signal entropy [13], [14]. Based on the m-PPM signals with different slot numbers (slot rates), a 12-dB rate-scaling range from 78 (38) Mbps to 1.25 Gbps (622 Mbps) was realized [6], [9]. Based on the burst-rate DPSK signals, a 16-dB rate-scaling range from 72 Mbps to 2.88 Gbps was demonstrated experimentally [11]. Another experimental demonstration using burst-rate DSPK achieved a 30-dB rate-scaling range from 2.4 Mbps to 2.5 Gbps [12]. However, these schemes affect the optical signal peak power, and thus may incur nonlinear impairments due to the high-power boost optical amplifier in the transmitter [12]. Based on the m-PSK signals with variable modulation orders, a 3-dB rate-scaling range was achieved [7]. Recently, based on the PCS-64QAM signals with variable shaping-parameters a 1.76-dB continuous rate-scaling range from 400 Gbps to 600 Gbps has been demonstrated experimentally [13], [14]. However, changing the modulation order and PCS entropy may affect the operation of the coherent receiver DSP algorithms [15]–[17]. Furthermore, for the long-reach photon-starving FSOC, lower-order mPSK signals, such as binary-phase-shift keying (BPSK) and quadrature-phase-shift keying (QPSK), are preferred to ensure a higher sensitivity [18], thus limiting the rate-scaling ranges of these schemes. In [7], a 5.6-dB rate-scaling range was obtained by changing the FEC code rate from 9/10 to 1/4. But it also has a limited rate-scaling range and has to be used with other techniques to achieve a large rate-scaling range.

Recently, the temporal diversity coherent combining (TDCC) has demonstrated its feasibility to realize an ultra-wide rate-scaling range without changing the signal pulse profile or modulation format [7]. Experimental results show that by block-repeating and coherent combining of a BPSK signal in a coherent receiver, a 45.6-dB rate-scaling range can be achieved. The working principle is simple. The N repeated blocks can be combined coherently for an improvement in the signal-to-noise ratio (SNR) by a factor of N if the phases of the optical field samples in the N blocks are aligned. By selecting N, the data-rate and loss tolerance can be traded for each other to adapt to different scenarios. However, the TDCC method proposed in [7] can not work in practice because the local oscillator (LO) frequency offset (LFO) and laser phase noise (LPN) were not considered and in the demonstration the transmitter and receiver were in an autodyne configuration using the same laser as the optical carrier and LO. In the practical FSOC system, the phase offsets between the samples to be combined change with time due to the LFO and LPN and will make the coherent combining unrealizable [19].

As far as we know, the method of implementing the TDCC in practical digital coherent receivers has not yet been investigated. To solve this problem, in this paper, we investigate the relationships between the computational complexity, optical phase alignment error, combining loss and data rate for the TDCC-based variable data-rate system. Analytical expressions revealing the relationships are deduced. Based on the analytical expressions, we propose an efficient method to implement the TDCC in practical digital coherent receivers with LFO, LPN and limited DSP resources by minimizing the computational complexity while achieving the expected output OSNR and the highest available data-rate for an arbitrary input OSNR. Both numerical simulations and experiments are carried out to validate the results obtained. The paper is organized as follows. The relationships between the computational complexity, optical phase alignment error and the combining loss are discussed in Section II. The method to minimize the computational complexity while achieving the maximal available data-rate is presented in Section III. Conclusions are drawn in Section IV.

II. PHASE ALIGNMENT ERROR AND COMBINING LOSS

Fig. 1(a) shows the setup of the FSOC system based on the digital coherent techniques [7], [20]. Fig. 1(b) shows the transmitted data block designed for the TDCC-based system. Each data block has the same length of L and is repeated N times [7]. In the coherent receiver, the weak optical signal is first coupled into a single-mode fiber and then amplified by a low-noise preamplifier to compensate for the large free-space transmission loss. An optical band-pass filter (OBPF) is used to mitigate the out-of-band amplified spontaneous emission (ASE) noise generated by the optical amplifier [20]. The input pre-amplified optical signal is detected by the integrated coherent receiver (ICR) and then input into the digital signal processing (DSP) system. Fig. 1(c) shows the DSP flow chart in detail. In the DSP, after front-end distortion compensation and clock recovery, the signal blocks are aligned in phase and then coherently combined to enhance the SNR. Then, the standard adaptive equalization and carrier recovery algorithms are applied to recover the transmitted symbols [21].

Fig. 2 shows the flow chart of the phase alignment and coherent combining process [22]. It operates by starting with the first signal block and coherently combining each signal block with a running coherent sum of all previous signal blocks. To realize the coherent sum, the optical phase offset (OPO) (φ_k) between the two signal blocks (S_n, S_{n+1}) consisting of the same symbol sequences to be added must be estimated first, so that the OPO can be compensated before the coherent addition. The OPO estimation can be realized blindly or with the help of pilot symbols and frame synchronization algorithms able to locate them under very lower OSNR [22], [23]. To average out the error induced by the large ASE noise, the OPO can be estimated by the following equations [22]

$$C_{sum} = \sum_{m=1}^{M} S_n[m] \cdot S_{n+1}^{*}[m], \tag{1}$$

$$\widehat{\varphi}_k = \arg\{C_{sum}\} = \varphi_k + \Delta\varphi_k. \quad (1 \le k \le N-1) \tag{2}$$

Here, $S_n[m]$ and $S_{n+1}[m]$ stand for the m-th samples of the two signal blocks to be coherently combined, respectively. M stands for the number of samples used for the OPO estimation. $\widehat{\varphi}_k$, φ_k and $\Delta\varphi_k$ stand for the estimated OPO, real OPO

and the corresponding estimation error, respectively. N represents the total number of blocks to be combined. As shown in Fig. 2, phase alignment can be realized by multiplying the signal S_{n+1} with $\exp(j\widehat{\varphi}_k)$ to mitigate the OPO. In practice, the practical combining gain is smaller than the ideal combining gain because $\Delta\varphi_k \neq 0$. Here, we define the combining efficiency (R) as the ratio of the practical SNR to the ideal SNR after the coherent combining. Then, the combining loss in dB unit can be written as $CL = -10\log_{10} R$ [24], [25].

According to (1) and (2), to balance the two competing requirements of low computational complexity and high estimation accuracy, M is the key parameter that should be chosen appropriately [20]. To investigate the relation between CL and M, we can begin with estimating the OPO between the first two signal blocks (S_1, S_2) represented by

$$S_1[m] = A_1 \exp\left[j\left(2\pi\Delta f m T_s + \phi_s + \phi_p(m)\right)\right] + n(m), \quad (1 \le m \le L) \tag{3}$$

$$S_2[m] = A_2 \exp\left[j\left(2\pi\Delta f (m+L) T_s + \phi_s + \phi_p(m+L)\right)\right] + n(m+L). \quad (1 \le m \le L) \tag{4}$$

Here, A_1 and A_2 stand for the amplitudes of the two signal blocks, respectively. Δf represents the LFO. T_s represents the sampling interval. L represents the block length. ϕ_s and ϕ_p stand for the modulated signal phase and LPN, respectively. $n(m)$ and $n(m+L)$ are the ASE noises following complex Gaussian distribution. The real and imaginary components of the ASE noise are independent identically distributed (i.i.d) random variables following Gauss distribution $N(0, \sigma_i^2)$ ($i = 1, 2$) [20]. The variance σ_i^2 is related to the electrical and optical signal-to-noise ratio (SNR_i and $OSNR_i$) by the following equation [25]

$$\frac{A_i^2}{2\sigma_i^2} = SNR_i = OSNR_i \times \gamma. \tag{5}$$

Here, γ is a calibration factor related to the signal bandwidth and modulation format [20]. Substituting (3) and (4) into (1) we can obtain

$$\begin{aligned} C_{sum} &= \sum_{m=1}^{M} S_1[m] \cdot S_2^*[m] \\ &= \sum_{m=1}^{M} \left\{ \begin{array}{l} \left[A_1 e^{j(2\pi\Delta f m T_s + \phi_s + \phi_p(m))} + n(m)\right] \\ \cdot \left[A_2 e^{j(2\pi\Delta f (m+L) T_s + \phi_s + \phi_p(m+L))} + n(m+L)\right]^* \end{array} \right\} \\ &= \sum_{m=1}^{M} \left\{ \begin{array}{l} A_1 A_2 e^{j[-2\pi\Delta f L T_s + \phi_p(m) - \phi_p(m+L)]} \\ + A_1 \tilde{n}^*(m+L) + A_2 \tilde{n}(m) + n(m) \cdot n^*(m+L) \end{array} \right\} \\ &= A_1 A_2 e^{j\varphi_1} \sum_{m=1}^{M} e^{-j\Delta\varphi_p(m)} + n_C. \end{aligned} \tag{6}$$

Here, $\varphi_1 = -2\pi\Delta f L T_s$ is the LFO-induced OPO (LFO-OPO) between the two signal blocks. $\Delta\varphi_p(m) = \phi_p(m+L) - \phi_p(m)$ represents the LPN-induced OPO (LPN-OPO). It is worth noting that the LPN $\phi_p(m)$ can be modeled by a Wiener process, and thus $\Delta\varphi_p(m)$ are i.i.d. Gaussian random variables with mean zero and the variance of $\sigma_{\Delta\varphi_p}^2 = 2\pi L \Delta v T_s$ [26], [27]. Here, Δv stands for the total 3-dB laser linewidth of the transmitter and LO lasers.

In the TDCC system, we generally use a large number of samples (M) to average out the ASE noise impact in the OPO estimation and lasers with a narrow linewidth (Δv) to reduce the LPN [7], [25]. In this case, the phase and amplitude of $\sum_{m=1}^{M} e^{-j\Delta\varphi_p(m)}$ can be approximated to zero and M, respectively, and thus C_{sum} is approximately equal to

$$C_{sum} \approx M A_1 A_2 e^{j\varphi_1} + n_C. \tag{7}$$

Here, n_C is the noise term and has the following form

$$n_C = \sum_{m=1}^{M} \left\{ A_1 \tilde{n}^*(m+L) + A_2 \tilde{n}(m) + n(m) \cdot n^*(m+L) \right\}. \tag{8}$$

Here, n_C can be approximated as a complex Gaussian random variable [24]. The real and imaginary components of n_C are i.i.d. random variables following Gauss distribution $N(0, \sigma_C^2)$ [25], where

$$\sigma_C^2 = M\left\{A_2^2\sigma_1^2 + A_1^2\sigma_2^2 + 2\sigma_2^2\sigma_1^2\right\}. \tag{9}$$

Thus, (7) can be rewritten as [24], [28]

$$C_{sum} \approx |C_{sum}| e^{j(\varphi_1 + \Delta\varphi_{n1})}. \tag{10}$$

Here $\Delta\varphi_{n1}$ is the so-called additive observation phase noise (AOPN) [29]. It can be approximated to a Gaussian random variable with mean zero and the variance given by [29]

$$\begin{aligned} \sigma_{\Delta\varphi_{n1}}^2 &\approx \frac{\sigma_C^2}{M^2 A_1^2 A_2^2} = \frac{A_2^2\sigma_1^2 + A_1^2\sigma_2^2 + 2\sigma_2^2\sigma_1^2}{M A_1^2 A_2^2} \\ &= \frac{1}{M}\left(\frac{1}{2SNR_1} + \frac{1}{2SNR_2} + \frac{1}{2SNR_1 \cdot SNR_2}\right) \\ &= \frac{1}{M}\left(\frac{1}{2\gamma OSNR_1} + \frac{1}{2\gamma OSNR_2} + \frac{1}{2\gamma^2 OSNR_1 \cdot OSNR_2}\right). \end{aligned} \tag{11}$$

Therefore, the estimated LFO-OPO can be written as

$$\widehat{\varphi}_1 = \arg\{C_{sum}\} = \varphi_1 + \Delta\varphi_{n1}. \tag{12}$$

To mitigate the LFO-OPO before coherent combining, S_2 is multiplied with $\exp(j\widehat{\varphi}_1)$ and we can get

$$\begin{aligned} S_2'[m] &= S_2[m] \cdot e^{j(\varphi_1 + \Delta\varphi_{n1})} \\ &= A_2 \exp\left[j\left(2\pi\Delta f m T_s + \phi_s + \Delta\varphi_{n1} + \phi_p(m+L)\right)\right] \\ &\quad + n'(m+L). \end{aligned} \tag{13}$$

Comparing (13) with (3), we can see that the phase alignment error between the two samples to be combined is

$$\begin{aligned} \Delta\varphi_1(m) &= \Delta\varphi_{n1} + \phi_p(m+L) - \phi_p(m) \\ &= \Delta\varphi_{n1} + \Delta\varphi_{p1}(m). \quad (1 \le m \le L) \end{aligned} \tag{14}$$

Since $\Delta\varphi_{n1}$ and $\Delta\varphi_{p1}$ are independent of each other and both of them follow Gaussian distribution [26], $\Delta\varphi_1(m)$ is

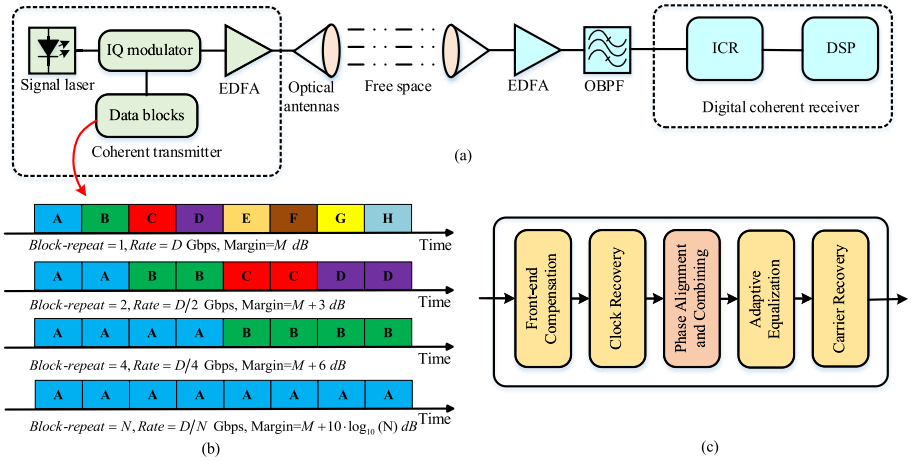

FIGURE 1. (a) The setup of the coherent FSOC system. (b) Block repeating and coherent combining concepts [7]. Letters A–H represent unique blocks of symbols. (c) DSP flow chart.

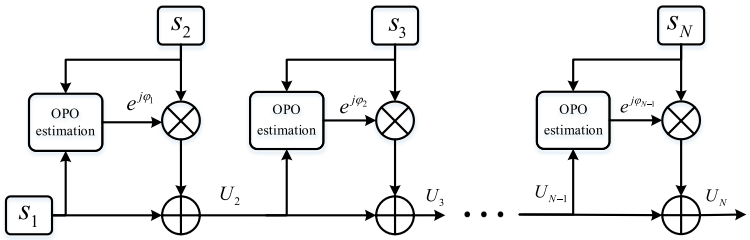

FIGURE 2. The phase alignment and digital coherent combining process proposed in [22].

also a Gaussian random variable. It has a zero mean and a variance of

$$\begin{aligned}\sigma^2_{\Delta\varphi 1} &= \sigma^2_{\Delta\varphi n1} + \sigma^2_{\Delta\varphi p1} = \frac{A_2^2\sigma_1^2 + A_1^2\sigma_2^2 + 2\sigma_2^2\sigma_1^2}{MA_1^2A_2^2} \\ &\quad + 2\pi L\Delta\nu T_s \\ &= \frac{1}{M}\left(\frac{1}{2\gamma OSNR_1} + \frac{1}{2\gamma OSNR_2}\right. \\ &\quad \left. + \frac{1}{2\gamma^2 OSNR_1 \cdot OSNR_2}\right) + 2\pi L\Delta\nu T_s. \end{aligned} \tag{15}$$

After the LFO-OPO is compensated, the two samples are coherently combined. The amplitude of the output signal can be written as

$$\begin{aligned} A_{U2} &= \left|A_1 + A_2 e^{j\Delta\varphi_1}\right| \\ &= \sqrt{(A_1 + A_2)^2 - 2A_1A_2\left(1 - \cos\Delta\varphi_1\right)} \\ &= \sqrt{(A_1 + A_2)^2 - 4A_1A_2\sin^2\left(\frac{\Delta\varphi_1}{2}\right)}. \end{aligned} \tag{16}$$

In general, the phase alignment error $\Delta\varphi_1$ is small, so (16) can be rewritten as

$$A_{U2} \approx \sqrt{(A_1 + A_2)^2 - A_1A_2\Delta\varphi_1^2}. \tag{17}$$

Thus, the combining efficiency R of the two blocks can be written as

$$\begin{aligned} R &= \left|\frac{A_1 + A_2 e^{j\Delta\varphi_1}}{A_1 + A_2}\right|^2 \approx \left|\frac{\sqrt{(A_1 + A_2)^2 - A_1A_2\Delta\varphi_1^2}}{A_1 + A_2}\right|^2 \\ &= 1 - \frac{A_1A_2\Delta\varphi_1^2}{(A_1 + A_2)^2}. \end{aligned} \tag{18}$$

The averaged R can thus be written as [24]

$$\begin{aligned} E\left(R\right) &= 1 - \frac{A_1A_2\sigma^2_{\Delta\varphi_1}}{(A_1 + A_2)^2} \\ &= 1 - \frac{A_1A_2}{(A_1 + A_2)^2} \times \left[\frac{1}{M}\left(\frac{1}{2\gamma OSNR_1} + \frac{1}{2\gamma OSNR_2}\right.\right. \\ &\quad \left.\left. + \frac{1}{2\gamma^2 OSNR_1 \cdot OSNR_2}\right) + 2\pi L\Delta\nu T_s\right] \end{aligned} \tag{19}$$

In practice, the FSOC systems are affected by the unwanted effects of atmospheric turbulence (AT) and boresight pointing errors (PE). The received signal power can fluctuate over the millisecond-class time scales due to the AT [7], [30] and over the second-class time scales due to the PE, respectively [31], [32]. However, the total duration of the N data blocks to be combined in the TDCC process is often on the order of a microsecond as the data rate is generally high and on the order of 10 Gbps for the coherent FSOC systems [7], [30]. Because

the AT and PE induced signal power and OSNR variations are relatively much slower, we can neglect the AT and PE impact and assume the OSNR of the N data blocks to be combined is the same, i.e. $OSNR_1 = OSNR_2 = \cdots = OSNR_N, A_1 = A_2 = \cdots = A_N$ and $\sigma_1 = \sigma_2 = \cdots = \sigma_N$. In this case, the equal gain combining (EGC) is the optimal choice, as it has the same combining gain as the maximum ratio combining (MRC) [20]. Therefore, the averaged R for the first coherent combining can be rewritten as

$$\begin{aligned} E(R_1) &= 1 - \frac{1}{4}\sigma^2_{\Delta\varphi_1} \\ &= 1 - \frac{1}{4}\left[\frac{1}{M_1}\left(\frac{1}{\gamma OSNR} + \frac{1}{2(\gamma OSNR)^2}\right) + 2\pi L\Delta\nu T_s\right]. \end{aligned} \tag{20}$$

Here, M_1 stands for the number of samples used for the OPO estimation for the first combining. After the first coherent combining, the averaged amplitude A_{U2} and OSNR of the output signal can be written as

$$A_{U2} = 2\sqrt{R_1}A_1, \tag{21}$$

$$OSNR_{U2} = R_1 \cdot (OSNR_1 + OSNR_2) = 2R_1 \cdot OSNR. \tag{22}$$

For the i-th $(1 \le i \le N-1)$ combining, the averaged combining efficiency R_i can be obtained by using the above method recursively. After some straight-forward algebra and simplification, the expressions of the averaged $R_i, A_{U(i+1)}$ and $OSNR_{U(i+1)}$ have the following forms

$$\begin{aligned} &E(R_i) \\ &= 1 - \frac{B_i}{(B_i+1)^2} \cdot \left[\frac{1}{M_i}\left(\frac{1}{2\gamma OSNR} + \frac{1}{2D_i\gamma OSNR} + \frac{1}{2D_i(\gamma OSNR)^2}\right) + \frac{i+1}{2i} \cdot 2\pi L\Delta\nu T_s\right], \\ &\qquad (1 \le i \le N-1) \end{aligned} \tag{23}$$

$$\begin{aligned} &A_{U(i+1)} \\ &= B_{i+1} \cdot A_1, \quad (1 \le i \le N-1) \end{aligned} \tag{24}$$

$$\begin{aligned} &OSNR_{U(i+1)} \\ &= D_{i+1} \cdot OSNR. \quad (1 \le i \le N-1) \end{aligned} \tag{25}$$

where

$$B_{i+1} = \prod_{l=1}^{i}\sqrt{R_l} + \sum_{j=1}^{i}\prod_{l=j}^{i}\sqrt{R_l} = \sqrt{R_i}(B_i+1), \quad (1 \le i \le N-1) \quad \text{and} \quad B_1 = 1. \tag{26}$$

$$D_{i+1} = \prod_{l=1}^{i}R_l + \sum_{j=1}^{i}\prod_{l=j}^{i}R_l = R_i(D_i+1), \quad (1 \le i \le N-1) \quad \text{and} \quad D_1 = 1. \tag{27}$$

Here, $M_i\,(1 \le i \le N-1)$ stands for the number of samples used in the OPO estimation for the i-th combining. $B_{i+1}\,(1 \le i \le N-1)$ represents the practical amplitude gain after temporal coherent combining of $(i+1)$ block repeats. $D_{i+1}\,(1 \le i \le N-1)$ represents the practical combining gain after temporal coherent combining of $(i+1)$ block repeats.

In summary, with (23) - (27) we can estimate the averaged output OSNR and the averaged R (CL) when the values of the input OSNR ($OSNR_{in}$), total laser linewidth $\Delta\nu$, sample number M_i, block length L and number of blocks N are known.

According to (23), the averaged CL_i of the i-th combining can be written as

$$\begin{aligned} &E(CL_i) \\ &= -10\lg[E(R_i)] \\ &= -10\lg\left\{1 - \frac{B_i}{(B_i+1)^2} \times \left[\frac{1}{M_i}\left(\frac{1}{2\gamma OSNR} + \frac{1}{2D_i\gamma OSNR} + \frac{1}{2D_i(\gamma OSNR)^2}\right) + \frac{i+1}{2i} \cdot 2\pi L\Delta\nu T_s\right]\right\} \\ &= -10\lg(1-\xi). \ (1 \le i \le N-1) \end{aligned} \tag{28}$$

where

$$\xi = \frac{B_i}{(B_i+1)^2}\left[\frac{1}{M_i}\left(\frac{1}{2\gamma OSNR} + \frac{1}{2D_i\gamma OSNR} + \frac{1}{2D_i(\gamma OSNR)^2}\right) + \frac{i+1}{2i} \cdot 2\pi L\Delta\nu T_s\right]. \tag{29}$$

For the typical values assigned to M_i and $\Delta\nu$, ξ is very small and becomes even smaller as i increases. For example, assuming $OSNR_{in} = -8\ dB$, $\Delta\nu = 10\ kHz$, $M_i = 30$ and $L = 2048$, the values of ξ are 0.058, 0.012 and 0.005, respectively, when i is 1, 5 and 10. According to the Taylor expansion, when $\xi \ll 1$

$$\lg(1-\xi) = \frac{-1}{\ln 10}\left\{\xi + \frac{\xi^2}{2} + \frac{\xi^3}{3} + \cdots + \frac{\xi^n}{n}\right\} \approx \frac{-1}{\ln 10}\xi. \tag{30}$$

Thus, (28) can be rewritten as

$$\begin{aligned} &E(CL_i) \\ &\approx \frac{10}{\ln 10} \cdot \frac{B_i}{(B_i+1)^2} \times \left[\frac{1}{M_i}\left(\frac{1}{2\gamma OSNR} + \frac{1}{2D_i\gamma OSNR} + \frac{1}{2D_i(\gamma OSNR)^2}\right) + \frac{i+1}{2i} \cdot 2\pi L\Delta\nu T_s\right] \\ &= CL_{ASE(i)} + CL_{PN(i)}, \end{aligned} \tag{31}$$

where

$$\begin{aligned} &CL_{ASE(i)} \\ &= \frac{10}{\ln 10}\frac{B_i}{(B_i+1)^2} \times \left[\frac{1}{M_i}\left(\frac{1}{2\gamma OSNR} + \frac{1}{2D_i\gamma OSNR} + \frac{1}{2D_i(\gamma OSNR)^2}\right)\right], \quad (1 \le i \le N-1) \end{aligned} \tag{32}$$

$$\begin{aligned} &CL_{PN(i)} \\ &= \frac{10}{\ln 10}\frac{B_i}{(B_i+1)^2} \cdot \frac{i+1}{2i} \cdot 2\pi L\Delta\nu T_s. \quad (1 \le i \le N-1) \end{aligned} \tag{33}$$

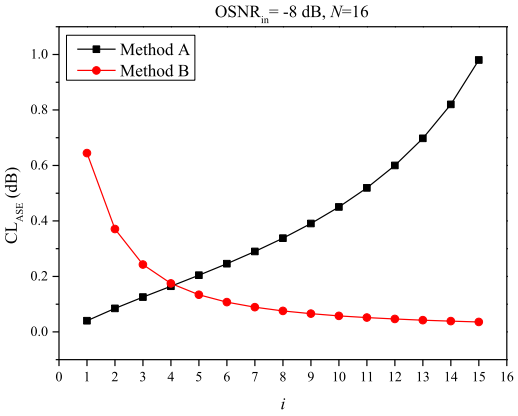

FIGURE 3. The variations of CL_{ASE} as a function of the times of coherent combining.

Here, $CL_{ASE(i)}$ and $CL_{PN(i)}$ represent the combining losses of the i-th combining incurred by the ASE noise and the LPN, respectively. As we can see, $CL_{ASE(i)}$ is inversely proportional to $OSNR_{in}$ and M. On the other hand, $CL_{PN(i)}$ is proportional to the product of $\Delta\nu$ and L. It is worth noting that $CL_{PN(i)}$ can be reduced by using a narrow linewidth laser or short data block. While $CL_{ASE(i)}$ can be mitigated by the phase alignment algorithm (PAA).

We note that, as the LFO-OPO increases linearly with time, it can also be mitigated by multiplying the data block with $\exp(j \cdot i\widehat{\varphi}_1) = \exp[j(i\varphi_1 + i\Delta\varphi_{n1})]$ before the i-th coherent combining. This method only needs one OPO estimation (hereinafter referred to as method A), while the method shown in Fig. 2 needs $N-1$ OPO estimation (hereinafter referred to as method B). However, as the phase alignment error $i\Delta\varphi_{n1}$ due to the ASE noise also increases with i, the performance of method A will be greatly degraded after several times of coherent combinations, especially when $OSNR_{in}$ is very low and $\Delta\varphi_{n1}$ is relatively large. The combining loss incurred by the ASE noise obtained with method A is given by

$$CL'_{ASE(i)} = \frac{10}{\ln 10}\frac{B_i}{(B_i+1)^2} \times \left[\frac{i^2}{M_i}\left(\frac{1}{2\gamma OSNR} + \frac{1}{2\gamma OSNR} + \frac{1}{2\,(\gamma OSNR)^2}\right)\right]. \quad (1 \le i \le N-1) \qquad (34)$$

As we can see, it increases quadratically with i. By contrast, with method B, the phase alignment error keeps decreasing with i as the OSNR keeps increasing with i. Fig. 3 shows the variations of $CL_{ASE(i)}$ predicted by (32) and (34) as a function of i, respectively. Here, $OSNR_{in} = -8\ dB$, $N = 16$. To compare the two methods fairly, the total samples used for the OPO estimation are the same. For method A, M is set to be 300, while for method B, M_i $(1 \le i \le 15)$ is set to be 20. As we can see, the results are consistent with the above predictions. After 15 times combining, the CL of method B is much lower.

To validate the analytical expressions presented, we compare the output OSNR calculated by the analytical expressions and numerical simulations for different combinations of M and N. Without loss of generality, we carried out the numerical simulations in a 10 Gbps QPSK TDCC-based system. The receiver setup is similar to that shown in Fig. 1. The fixed simulation parameters are shown in Table 1. Hereinafter, they keep unchanged. Fig. 4(a) shows the variations of the averaged output OSNR obtained by (23) - (27) as a function of M and N when $OSNR_{in} = -6\ dB$. Fig. 4(b) shows the averaged output OSNR obtained from 1000 times of Monte Carlo simulations with different ASE noise patterns. Fig. 4(c) shows the difference between the analytical and numerical results. As we can see, the difference is lower than 0.1 dB in most areas, showing the results obtained with the analytical expressions agree well with the results obtained by numerical simulations.

TABLE 1. Simulation parameters.

Parameter	Unit	Value
Laser Frequency Offset	MHz	500
Laser Linewidth $\Delta\nu$	kHz	10
Block Length L	Sample	2048

III. OPTIMIZATION OF COMPUTATIONAL COMPLEXITY

As the effort for a real multiplier is much higher than for an adder, the number of real multiplications required is used as the figure of merit to measure the complexity of the PAA in this paper. The computational complexity of the PAA can be measured by the number of real multiplications required per sample which is given by

$$\frac{4\sum_{i=1}^{N-1} M_i + 4L(N-1)}{L} = \frac{4\sum_{i=1}^{N-1} M_i}{L} + 4(N-1). \qquad (35)$$

The above analytical expressions reveal the relationships between the computational complexity, optical phase alignment error and the CL for the TDCC-based variable data-rate coherent FSOC system. They can help us minimize the computational complexity while achieving the expected output OSNR and the highest available data-rate for an arbitrary $OSNR_{in}$.

As explained above, M_i is a key parameter to balance the competing requirements between the low computational complexity and the low phase alignment error (small combining loss). Furthermore, M_i also affects the error-free transmission data-rate. If M_i is too small, a large phase alignment error occurs, and thus it will take more times of combining to reach the OSNR threshold, thus reducing the data-rate. There are two methods for choosing M_i. The first method is fixing M_i for all combinations, i.e. $M_i = M$, $(1 \le i \le N-1)$. It is simple and convenient for practical implementation. The second method is using different M_i for each time of the combinations to guarantee the expected combining loss CL_i. For example, at the very beginning of the $N-1$ times of

combinations, the OSNR of the signals to be combined is low, and thus we can choose a larger M_i. While, when the OSNR increases after repeated combinations, we can choose a smaller M_i.

To compare the two methods fairly, we compare the output OSNR of the two methods when their computational complexities are the same. Without loss of generality, we assume that $OSNR_{in} = -8\ dB$, $N = 32$ and the expected CL_i for the second method is 0.1 dB. M_i for the second method is calculated by (23) - (27). Therefore, we can obtain the total samples used for the OPO estimations. Here, the number of the total samples is 532. In order to ensure the same computational complexity, we can set M_i to be $532/31 \approx 17$ for the first method. Then we can calculate the averaged output OSNR and CL_i with (23) - (27). Fig. 5(a) shows the variations of the M_i and CL_i as a function of i, respectively. Fig. 5(b) shows the variations of the output OSNR as a function of i. As we can see, when i is small, the second method has better performance in terms of the CL and output OSNR as it uses a larger M_i at the beginning. However, when i becomes larger, the opposite is true. This is because CL_i keeps decreasing with the first method, while it keeps fixed for the second method. As a result, when N approaches 32, the first method has better performance than the second method in terms of the CL and output OSNR. Fig. 5(c) shows the variations of the output OSNR improvement of the first method as a function of N when the two methods have the same computational complexity. As we can see, the larger N is, the greater the advantage of the first method. When N is 32 and 64, the OSNR improvement is about 0.8 and 1.8 dB, respectively. In summary, the first method has better performance than the second method and is easier to implement. Therefore, we use the first method hereinafter.

When the values of $OSNR_{in}$, Δv, L and the expected output OSNR (or the error-free OSNR threshold) are known, we can calculate the values of M and N by (23) - (27). For example, for the 10 Gbaud QPSK signal, the error-free threshold OSNR is about 8 dB [7], [33]. Therefore, the expected output OSNR is set to be 8 dB. When the values of Δv and L are known, we can obtain the various combinations of M and N for the expected output OSNR as shown in Fig. 6(a). Here, the simulation parameters are the same as in Table 1. As we can see, N decreases with increasing M, which means that a higher data-rate can be obtained when M is larger. This is because a larger M can reduce the CL, thus reducing the required times of coherent combinations to achieve the expected output OSNR. However, when M is very large, the curve flattens out. This is because, in this case, the phase alignment error and CL are already close to the theoretical limit, so the increase of M can't obviously improve the output OSNR, thus reducing N, any more. The lower limits for N in Fig. 6(a) are given by $N = \lceil 10^{(OSNR_{out} - OSNR_{in})/10} \rceil$, here $\lceil \cdot \rceil$ stands for the top integral function. Here, $\mathrm{OSNR_{in}}$ and $\mathrm{OSNR_{out}}$ are in dB units. In summary, there is a trade-off between the computation complexity and data-rate for the TDCC-based coherent receiver.

As for the first method, the computational complexity is given by $4\,(M + L)\,(N - 1)/L$. By substituting the values of M and N given in Fig. 6(a) into this equation, we can obtain the computational complexity as shown in Fig. 6(b). The corresponding data-rate is shown in Fig. 6(c). In Fig. 6(b), the points A, B, C and D stand for the (M, N) with the minimum computational complexity. In Fig. 6(c), the points B, C, D and E stand for the (M, N) with the highest data-rates. Here, the points labeled with the same letter stand for the same (M, N). When $OSNR_{in}$ is relatively large, the (M, N) with the minimum computational complexity also corresponds to the maximum data-rate, which is represented by points B, C and D. However, when $OSNR_{in}$ is very small, this is no longer true, as shown by points A and E in Fig. 6(c). However, the data-rate at point A is very close to the maximum data-rate at point E. The difference is about 2.4%. Here, we assume that reducing the computational complexity is of higher priority, and thus choose the (M, N) with the minimum complexity.

Fig. 7(a) shows the variations of M and N corresponding to the minimum computational complexity as a function of $OSNR_{in}$, respectively. As expected, M and N keep decreasing with increasing $OSNR_{in}$. Fig. 7(b) shows the corresponding computational complexity and data-rate. As we can see, the computational complexity decreases with increasing $OSNR_{in}$, while the data-rate increases with increasing $OSNR_{in}$. When $OSNR_{in}$ increases from -10 to 0 dB, the computational complexity is reduced by about 10.4 times, while the data-rate is increased by about 8.4 times. Fig. 7(c) shows the variations of the output OSNR obtained by analytical expression and Monte Carlo simulation as a function of $OSNR_{in}$. The blue line shows the difference between the analytical and numerical results. As we can see, the difference is less than 0.1 dB, indicating that the analytical results agree well with the numerical results.

Fig. 8(a) and shows the schematic diagram of the experimental setup. At the transmitter, an arbitrary waveform generator (AWG) with an electrical 3- dB bandwidth of 25 GHz and a sampling rate of 40 GSa/s is used to generate the analog signals corresponding to the in-phase and quadrature components of the 10 GBaud Nyquist QPSK signal shaped with a roll-off of 0.1. The analog signals are amplified and -used to drive an IQ modulator fed by a laser at 1550.278 nm with a linewidth of 10 kHz. The drive signal for the data IQ modulator is a $2^{13}-1$ length pseudorandom binary sequence (PRBS). In front of the receiver, a variable optical attenuator (VOA) and erbium-doped fiber amplifier (EDFA) are used to control the optical signal power and OSNR of the optical signal input into the receiver. An optical bandpass filter is used to mitigate the out-of-band ASE noise. The coherent receiver is a pseudo-single-side-band-signal-based single-photodiode coherent receiver (P-SCR) [33], [34]. A 3-dB optical coupler is used to combine the received optical signal with the LO at 1550.324 nm with a linewidth of 10 kHz. The polarization controller (PC) is used to adjust the polarization state of the modulated signal so that it is aligned

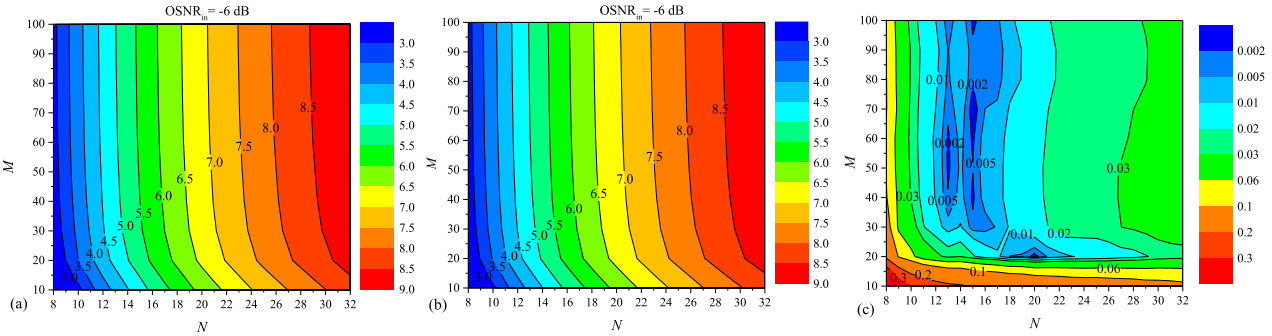

FIGURE 4. (a) and (b) show the variations of output OSNR obtained by analytical expressions and Monte Carlo simulations, respectively. (c) shows the difference between (a) and (b).

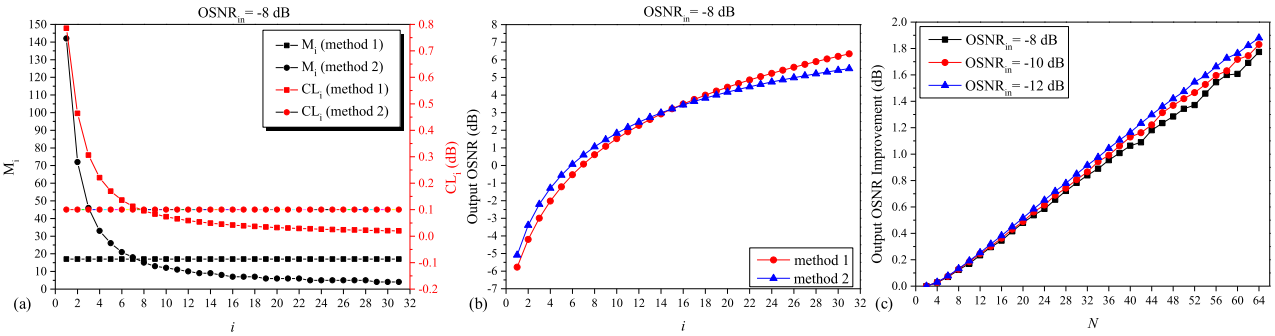

FIGURE 5. (a) Shows the variations of M_i, CL_i as a function of i, respectively, when $N = 32$. (b) shows the variations of the output OSNR as a function of i, when $N = 32$. (c) shows the variations of the output OSNR improvement of the first method as a function of N.

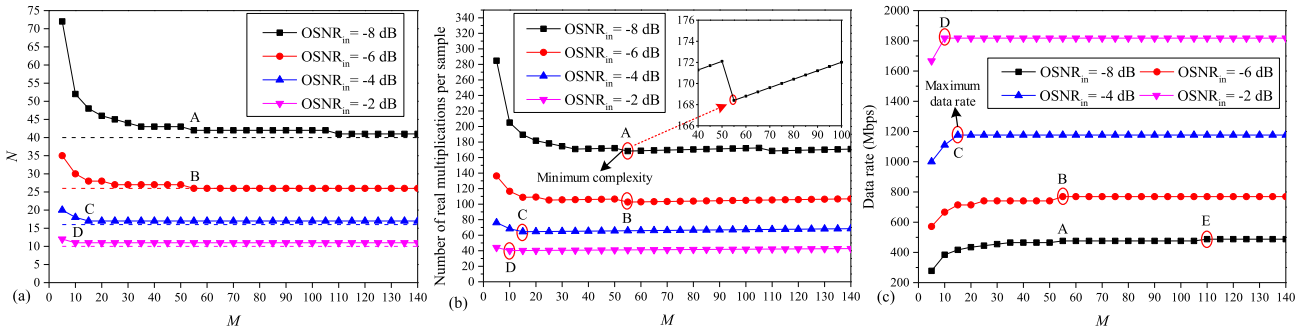

FIGURE 6. (a), (b) and (c) show the variations of the N, the computational complexity and data-rate as a function of M, respectively.

with the LO. A single-ended photodiode with a 20 GHz bandwidth is used to detect the optical signal. The detected AC electrical signals are sampled by a real-time oscilloscope with an electrical 3-dB bandwidth of 36 GHz and a sampling rate of 40 GSa/s. The sampled signals are stored and processed off-line by a computer. The flow chart of the DSP chain is also plotted in Fig. 8(b). After down-sampling to 2 samples per symbol, an optical field reconstruction algorithm is first used to recover the baseband complex signal [34]. The following algorithms are the same as Fig. 1.

Fig. 9(a) shows the variations of the output OSNR as a function of N when $OSNR_{in}$ is -1.3 dB, -4 dB, -6.2 dB and -8 dB, respectively. Both analytical and experimental results are plotted in Fig. 9(a) for comparison. Here, M is calculated by (23) - (27). For example, when $OSNR_{in}$ is -8 dB, the total laser linewidth is 20 kHz, the expected output OSNR is 8 dB, and the block length is $2^{13} - 1$, according to (23) - (27), (M, N) is (148, 42). With the same method, we can find that the values of (M, N) are (21, 9), (27, 17) and (52, 28), respectively, when $OSNR_{in}$ is -1.3 dB, -4 dB and -6.2 dB. As we can see from Fig. 9(a), the analytical and experimental results agree very well for all input OSNRs. Fig. 9(b) shows the constellation diagrams obtained when $N = 1$, 14, 28 and 42 and $OSNR_{in}$ is -8 dB. As we can see, the output OSNRs are 3.25 dB, 6.31 dB and 8.02 dB, respectively. The values calculated by analytical expression are 3.27 dB, 6.28 dB and 8.05 dB, respectively. The difference between the analytical and experimental results is less than 0.1 dB.

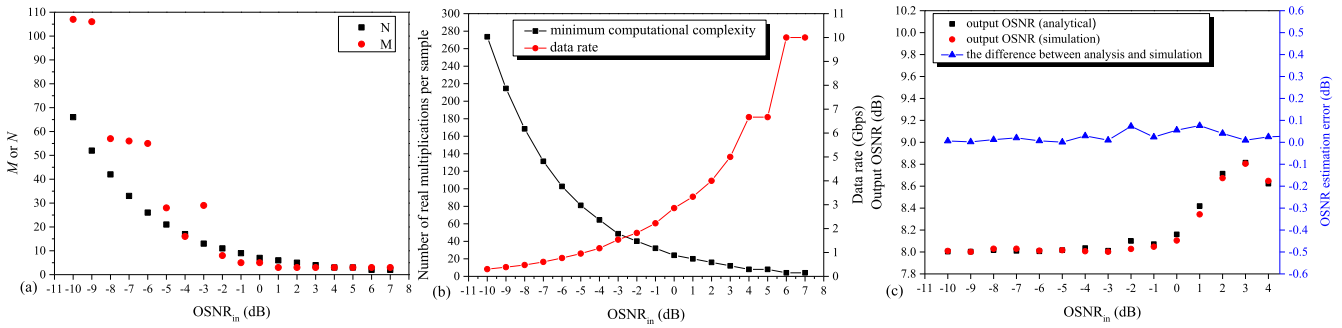

FIGURE 7. (a), (b) and (c) show the variations of N or M, the computational complexity and output OSNR as a function of $OSNR_{in}$, respectively.

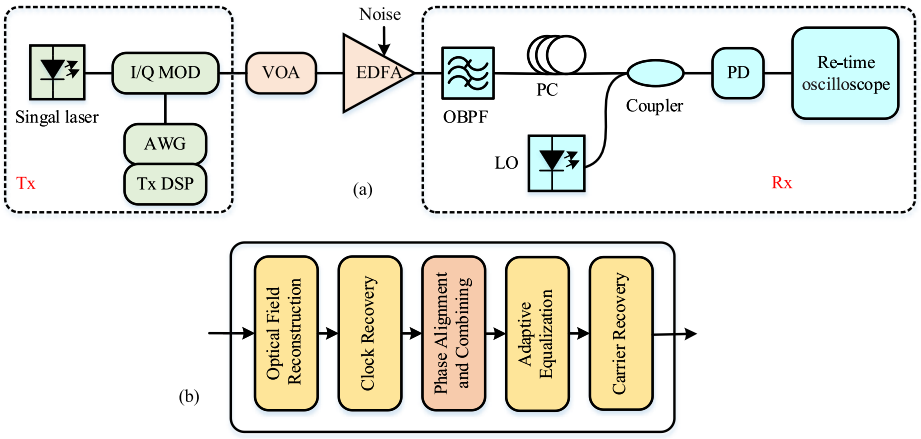

FIGURE 8. (a) Experimental Setup. (b) Flow chart of the DSP chain.

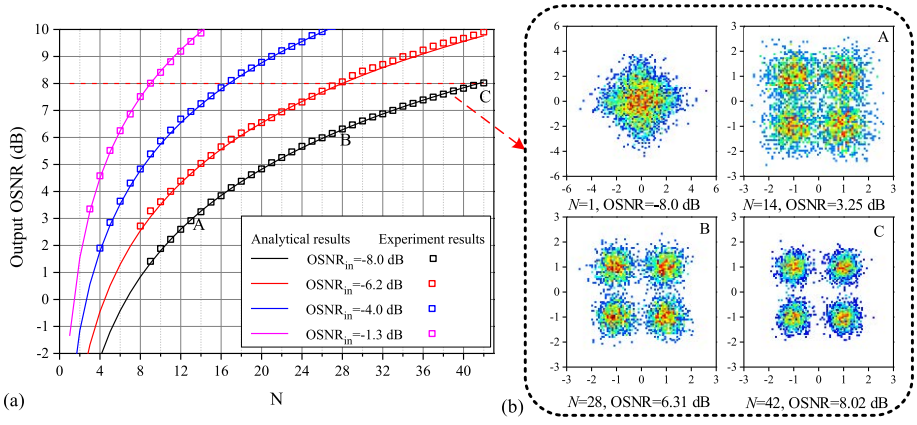

FIGURE 9. (a) The variations of the output OSNR as a function of the number of repeated blocks. (b) The constellation diagrams for $N = 1$, 14, 28 and 42, respectively, when $OSNR_{in} = -8$ dB.

IV. CONCLUSION

In this paper, we investigate the relationships between the computation complexity, optical phase alignment error, combining loss and data-rate for the TDCC-based rate-scaling technique. Analytical expressions are deduced to provide a simple procedure to find the desirous values for the number of samples used in the OPO estimation (M) and the required number of coherent combining (N) according to the input OSNR, laser linewidth $\Delta\nu$, block length L and expected output OSNR. It is found that with the same computation complexity, simply fixing the number of samples used in the OPO estimation achieves a higher output OSNR than fixing the combining loss in the whole TDCC procedure. We also find that, for a given input and output OSNR, there exists an optimal M that minimizes the computation complexity. When M is smaller than the optimal value, N becomes larger

leading to a higher computation complexity, while when M is larger than the optimal value, N has an asymptotic floor and the computation complexity increases with M. For the same reason, using a larger M than the optimal value only leads to a marginal improvement in the data-rate. The analytical results and proposed computation complexity optimization method are validated by numerical simulations and experimental results. This work can provide useful design tools and guidelines for low computation complexity TDCC-based variable data-rate FSOC systems. We note that we do not consider the AT and PE effects in the TDCC procedure as they are much slower than the TDCC procedure. At a much larger time scale, the AT- and PE-induced OSNR variations should be considered. In this case, one can adjust M and N periodically after every hundreds of times of TDCC procedures with the proposed method by monitoring the input signal OSNR. Due to space limitations, this issue will be discussed in our further work.

REFERENCES

[1] D. M. Boroson, B. S. Robinson, D. V. Murphy, D. A. Burianek, F. Khatri, J. M. Kovalik, Z. Sodnik, and D. M. Cornwell, "Overview and results of the lunar laser communication demonstration," *Proc. SPIE*, vol. 8971, pp. 1–11, Mar. 2014.

[2] D. M. Cornwell, "NASA's optical communications program for 2017 and beyond," in *Proc. IEEE Int. Conf. Space Opt. Syst. Appl. (ICSOS)*, New Orleans, LA, USA, Nov. 2017, pp. 10–14.

[3] H. Hemmati and D. O. Caplan, "Optical satellite communications," in *Optical Fiber Telecommunications VIB: Systems and Networks*, 6th ed. Amsterdam, The Netherlands: Elsevier, 2013, ch. 4, sec. 3, pp. 130–134.

[4] D. O. Caplan, "Laser communication transmitter and receiver design," *J. Opt. Fiber Commun. Rep.*, vol. 4, nos. 4–5, pp. 225–362, Sep. 2007.

[5] M. Toyoshima, "Trends in satellite communications and the role of optical free-space communications," *J. Opt. Netw.*, vol. 4, no. 6, pp. 300–311, May 2005.

[6] D. O. Caplan, B. S. Robinson, R. J. Murphy, and M. L. Stevens, "Demonstration of 2.5-Gslot/s optically-preamplified M-PPM with 4 photons/bit receiver sensitivity," in *OFC/NFOEC Tech. Dig. Opt. Fiber Commun. Conf.*, Anaheim, CA, USA, 2005, Paper PDP32.

[7] D. J. Geisler, C. M. Schieler, T. M. Yarnall, M. L. Stevens, B. S. Robinson, and S. A. Hamilton, "Demonstration of a variable data-rate free-space optical communication architecture using efficient coherent techniques," *Opt. Eng.*, vol. 55, no. 11, pp. 1–11, Aug. 2016, Art. no. 111605.

[8] X. Zhou, L. E. Nelson, P. Magill, R. Isaac, B. Zhu, D. W. Peckham, and K. Carlson, "High spectral efficiency 400 Gb/s transmission using PDM time-domain hybrid 32–64 QAM and training-assisted carrier recovery," *J. Lightw. Technol.*, vol. 31, no. 7, pp. 999–1005, Feb. 15, 2013.

[9] M. M. Willis, B. S. Robinson, M. L. Stevens, B. R. Romkey, J. A. Matthews, J. A. Greco, M. E. Grein, E. A. Dauler, A. J. Kerman, D. Rosenberg, D. V. Murphy, and D. M. Boroson, "Downlink synchronization for the lunar laser communications demonstration," in *Proc. Int. Conf. Space Opt. Syst. Appl. (ICSOS)*, Santa Monica, CA, USA, May 2011, pp. 83–87.

[10] N. W. Spellmeyer, S. L. Bernstein, D. M. Boroson, D. O. Caplan, A. S. Fletcher, S. A. Hamilton, R. J. Murphy, M. Norvig, H. G. Rao, B. S. Robinson, S. J. Savage, R. T. Schulein, M. L. Stevens, and J. P. Wang, "Demonstration of multi-rate thresholded preamplified 16-ary pulse-position-modulation," in *Proc. Opt. Fiber Commun. Conf.*, 2010, pp. 1–3.

[11] N. W. Spellmeyer, C. A. Browne, D. O. Caplan, J. J. Carney, M. L. Chavez, A. S. Fletcher, J. J. Fitzgerald, R. D. Kaminsky, G. Lund, S. A. Hamilton, R. J. Magliocco, O. V. Mikulina, R. J. Murphy, H. G. Rao, M. S. Scheinbart, M. M. Seaver, and J. P. Wang, "A multi-rate DPSK modem for free-space laser communications," *Proc. SPIE*, vol. 8971, pp. 130–138, Mar. 2014.

[12] D. O. Caplan, H. Rao, J. P. Wang, D. M. Boroson, J. J. Carney, A. S. Fletcher, S. A. Hamilton, R. Kochhar, R. J. Magliocco, R. Murphy, M. Norvig, B. S. Robinson, R. T. Schulein, and N. W. Spellmeyer, "Ultra-wide-range multi-rate DPSK laser communications," in *Proc. Conf. Lasers Electro-Opt.*, Mar. 2010, pp. 1–2.

[13] J. Cho and P. J. Winzer, "Probabilistic constellation shaping for optical fiber communications," *J. Lightw. Technol.*, vol. 37, no. 6, pp. 1590–1607, Mar. 15, 2019.

[14] F. P. Guiomar, A. Lorences-Riesgo, D. Ranzal, F. Rocco, A. N. Sousa, M. A. Fernandes, B. T. Brandao, A. Carena, A. L. Teixeira, M. C. R. Medeiros, and P. P. Monteiro, "Adaptive probabilistic shaped modulation for high-capacity free-space optical links," *J. Lightw. Technol.*, vol. 38, no. 23, pp. 6529–6541, Dec. 1, 2020.

[15] O. Bertran-Pardo, J. Renaudier, G. Charlet, H. Mardoyan, P. Tran, M. Salsi, and S. Bigo, "Overlaying 10 Gb/s legacy optical networks with 40 and 100 Gb/s coherent terminals," *J. Lightw. Technol.*, vol. 30, no. 14, pp. 2367–2375, May 24, 2012.

[16] M. Yan, Z. Tao, H. Zhang, W. Yan, T. Hoshida, and J. C. Rasmussen, "Adaptive blind equalization for coherent optical BPSK system," in *Proc. 36th Eur. Conf. Exhib. Opt. Commun.*, Turin, Italy, Sep. 2010, pp. 1–3.

[17] F. A. Barbosa, S. M. Rossi, and D. A. A. Mello, "Clock recovery limitations in probabilistically shaped transmission," in *Proc. Opt. Fiber Commun. Conf. (OFC)*, 2020, pp. 1–3, Paper M4J-4.

[18] S. Chandrasekhar, X. Liu, T. H. Wood, and R. W. Tkach, "High sensitivity modulation formats," in *Proc. Opt. Fiber Commun. Conf.*, 2012, pp. 1–3.

[19] S. Schaefer, M. Gregory, and W. Rosenkranz, "Digital frequency offset compensation in high-speed optical intersatellite data transmission systems," in *Proc. Eur. Conf. Opt. Commun. (ECOC)*, Valencia, Spain, Sep. 2015, pp. 1–3.

[20] C. Rao, S. Cui, Y. Tu, K. Zhou, and D. Liu, "Toward practical digital phase alignment for coherent beam combining in multi-aperture free space coherent optical receivers," *IEEE Access*, vol. 8, pp. 202585–202595, 2020.

[21] S. J. Savory, "Digital coherent optical receivers: Algorithms and subsystems," *IEEE J. Sel. Topics Quantum Electron.*, vol. 16, no. 5, pp. 1164–1179, Sep. 2010.

[22] D. J. Geisler, T. M. Yarnall, M. L. Stevens, C. M. Schieler, B. S. Robinson, and S. A. Hamilton, "Multi-aperture digital coherent combining for free-space optical communication receivers," *Opt. Exp.*, vol. 24, no. 12, pp. 12661–12671, Jun. 2016.

[23] Q. Cheng, S. Cui, K. Zhou, and D. Liu, "Training-aided joint frame and frequency synchronization for free space optical communication signals with low OSNR," *Opt. Commun.*, vol. 473, Oct. 2020, Art. no. 126046.

[24] J. Xiang and X. Lyu, "Statistical model of combining efficiency for digital phase alignment in multi-aperture free-space coherent optical receivers," in *Proc. IEEE 4th Int. Conf. Electron. Commun. Eng. (ICECE)*, Dec. 2021, pp. 252–260.

[25] Y. Tu, S. Cui, K. Zhou, and D. Liu, "Phase alignment with minimum complexity for equal gain combining in multi-aperture free-space digital coherent optical communication receivers," *IEEE Photon. J.*, vol. 12, no. 2, pp. 1–10, Apr. 2020.

[26] M.-W. Wu and P.-Y. Kam, "Soft-decision-aided, maximum-likelihood carrier phase estimation for coherent optical QAM," *J. Lightw. Technol.*, vol. 31, no. 22, pp. 3443–3452, Aug. 23, 2013.

[27] D. S. Millar, R. Maher, D. Lavery, T. Koike-Akino, M. Pajovic, A. Alvarado, M. Paskov, K. Kojima, K. Parsons, B. C. Thomsen, S. J. Savory, and P. Bayvel, "Design of a 1 Tb/s superchannel coherent receiver," *J. Lightw. Technol.*, vol. 34, no. 6, pp. 1453–1463, Mar. 15, 2016.

[28] Y. Li, M.-W. Wu, X. Du, T. Song, and P.-Y. Kam, "A refinement to the Viterbi-Viterbi carrier phase estimator and an extension to the case with a Wiener carrier phase process," *IEEE Access*, vol. 7, pp. 78170–78184, 2019.

[29] H. Fu and P.-Y. Kam, "Phase-based, time-domain estimation of the frequency and phase of a single sinusoid in AWGN—The role and applications of the additive observation phase noise model," *IEEE Trans. Inf. Theory*, vol. 59, no. 5, pp. 3175–3188, May 2013.

[30] D. J. Geisler, T. M. Yarnall, C. M. Schieler, M. L. Stevens, B. S. Robinson, and S. A. Hamilton, "Experimental demonstration of multi-aperture digital coherent combining over a 3.2-km free-space link," *Proc. SPIE*, vol. 10096, pp. 1–8, Feb. 2017.

[31] A. Jurado-Navas, J. M. Garrido-Balsells, J. F. Paris, M. Castillo-Vázquez, and A. Puerta-Notario, "Impact of pointing errors on the performance of generalized atmospheric optical channels," *Opt. Exp.*, vol. 20, no. 11, pp. 12550–12562, May 2012.
[32] M. R. Bhatnagar and Z. Ghassemlooy, "Performance analysis of Gamma–Gamma fading FSO MIMO links with pointing errors," *J. Lightw. Technol.*, vol. 34, no. 9, pp. 2158–2169, May 1, 2016.
[33] K. Zhou, S. Cui, Y. Gu, Y. Tu, C. Ke, and D. Liu, "Design of the real-time single-photodiode digital coherent receiver suitable for free space optical communication," *IEEE Photon. J.*, vol. 12, no. 5, pp. 1–12, Oct. 2020.
[34] K. Zhou, S. Cui, Y. Tu, and D. Liu, "A method to reduce the algorithm complexity of the single-photodiode-per-polarization coherent receiver," *IEEE Photon. J.*, vol. 12, no. 1, pp. 1–10, Feb. 2020.

FAMING LI was born in Yunnan, China, in 1995. He received the B.E. degree in optical and electronic information engineering from the Huazhong University of Science and Technology, China, in 2020. He is currently pursuing the M.S. degree in electronic information with the National Engineering Laboratory for Next Generation Internet Access System. His research interests include design and realization of low complexity and variable data-rate free space optical communication systems.

SHENG CUI received the Ph.D. degree in radio physics from Xidian University, Xi'an, China. He has been an Associate Professor with the School of Optical and Electronic Information, Huazhong University of Science and Technology, since 2011. His research interests include novel coherent detection, intelligent optical performance monitoring and distortion compensation techniques for free space, and fiber optical communication systems.

YANAN CHEN was born in Beijing, China, in 1980. He currently works with the Science and Technology on Electro-Optical Information Security Control Laboratory. His professional direction is optoelectronic information engineering.

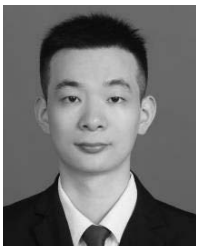

CHENJIE RAO was born in Jiangxi, China, in 1996. He received the B.E. degree in optical and electronic information engineering from the Huazhong University of Science and Technology, China, in 2018, and the M.S. degree in optical engineering, in 2021. He is currently working at Fiberhome Telecommunication Technologies. His research interests include design and realization of the low complexity and power consumption free space optical communication system.

YICONG TU was born in Nanchang, China, in 1994. He received the B.E. degree in optical and electronic information engineering from the Huazhong University of Science and Technology, China, in 2017, and the M.S. degree in optical engineering, in 2020. His research interests include free space optical communication technology and distortion compensation algorithms in digital coherent receivers.

KEJI ZHOU was born in Wuhan, China, in 1992. He received the M.S. degree from The University of Sheffield, Sheffield, U.K., in 2015. He is currently pursuing the Ph.D. degree in optical engineering with the Huazhong University of Science and Technology, Wuhan, China. He is also working at Fiberhome Telecommunication Technologies. His research interests include novel optical field reconstruction techniques and digital distortion compensation algorithms.

DEMING LIU received the Ph.D. degree in optical communication and optical network from the Huazhong University of Science and Technology, Wuhan, China. He is currently the Director of the National Engineering Laboratory of Next Generation Internet Access System for several years. His research interests include optical communication devices and systems, optical access and wireless access, optical sensing, and the Internet of Things.